Robust Spectral Denoising for Water-Fat Separation in Magnetic Resonance Imaging

Felix Lugauer[1], Dominik Nickel[2], Jens Wetzl[1], Stephan A. R. Kannengiesser[2], Andreas Maier[1], Joachim Hornegger[1]

[1] Pattern Recognition Lab, Friedrich-Alexander-Universitat Erlangen-Nürnberg
[2] MR Applications Predevelopment, Siemens Healthcare, Erlangen, Germany

Abstract. Fat quantification based on the multi-echo Dixon method is gaining importance in clinical practice as it can match the accuracy of spectroscopy but provides high spatial resolution. Accurate quantification protocols, though, are limited to low SNR and suffer from a high noise bias. As the clinically relevant water and fat components are estimated by fitting a non-linear signal model to the data, the uncertainty is further amplified. In this work, we first establish the low-rank property and its locality assumptions for water-fat MRI and, consequently, propose a model-consistent but adaptive spectral denoising. A robust noise estimation in combination with a risk-minimizing threshold adds to a fully-automatic method. We demonstrate its capabilities on abdominal fat quantification data from in-vivo experiments. The denoising reduces the fit error on average by 37 % and the uncertainty of the fat fraction by 58 % in comparison to the original data while being edge-preserving.

Keywords: Robust Denoising, Water-Fat MRI, Locally Low-Rank

1 Introduction

Tissue fat concentration is an established indicator for various disorders like hepatic steatosis or fatty liver disease. Even though liver biopsy is invasive and risk-involving, it is still widely used in clinical practice [1].

Recently, validated biomarkers, foremost the proton density fat fraction (PDFF), could be obtained non-invasively by MR spectroscopy (MRS) and MRI [2]. While the latter enables a larger coverage, it can only quantify the tissue fat concentration accurately when confounding effects like T_1 bias, R_2^* relaxation and magnet imperfections are sufficiently mitigated [3]. As a consequence, clinical fat quantification protocols based on MRI are limited in resolution and flip angle as to reduce T_1-bias and noise bias [4]. Also, a larger series of contrast images (e.g. 6 echos) must be acquired to enable the estimation of iron as well and to reduce the remaining confounding factors [5]. As this signal is used to determine the clinically relevant biomarkers by a non-linear voxel-wise fit, further noise amplification arises. Suppressing this noise—depending on breath-hold, resolution and flip angle parameters—by exploiting the shared information in the data series is desirable. However, typical priors promoting similarities of intensity or

gradient data cannot be enforced directly due to strong variations in contrast. Yet, in multi-contrast imaging there is a spectral sparsity when the number of modeled components is less than the acquired contrast images. Previously, this sparsity motivated the use of singular value filtering [6] for multi-echo denoising, assuming a low-rank (LR) signal. Advances in matrix completion [7] leveraged LR regularization based on the nuclear norm for various applications. [8] showed the benefit of local over global LR priors for dynamic MRI. Recently, extending the unbiased risk estimator for singular value thresholding (SVT) enables risk-minimizing denoising for a given noise estimate [9]. We adopt these concepts, and first show that the LR property of multi-contrast images is well-justified for local correlations of the signal, lending itself ideally for local processing. Then, the noise level of the signal is robustly estimated from local estimates which feeds an adaptive block-wise SVT. Our proposed method is validated both qualitatively and quantitatively using in-vivo experiments.

2   Water-Fat Imaging

Water-fat separation and quantification is based on the known difference of spectral properties between hydrogen nuclei bound in water and fat. An exact determination requires multiple echos for estimating and correcting the phase evolution $\boldsymbol{\Phi} \in \mathbb{C}^{N \times E}$ incorporating R_2^* relaxation, field inhomogeneities, gradient delays and eddy currents. The relation between the spectral components of water and fat and the e-th echo image $\boldsymbol{w}, \boldsymbol{f}, \boldsymbol{x}_e \in \mathbb{C}^N$ at time t_e is modeled as,

$$\boldsymbol{x}_e(j) = (\boldsymbol{w}(j) + c_{t_e}\boldsymbol{f}(j))\,\mathrm{e}^{\mathrm{i}\boldsymbol{\Phi}(j,e)}, \; j = 1 \ldots N, \; e = 1 \ldots E, \qquad (1)$$

for the j-th out of N voxels and E contrast images. A pre-calibrated multi-peak fat spectrum is given by $c_{t_e} \in \mathbb{C}$ while the phase effects are modeled with $\mathrm{e}^{\mathrm{i}\boldsymbol{\Phi}(j,e)}$.

Biomarker Estimation. The clinically relevant signals of water, fat and R_2^*—an indicator for increased iron deposits—are determined voxel-wise by a nonlinear fit of either the complex- or absolute-valued contrast images [10]. Then, the fat fraction (PDFF), an important biomarker, is simply $\boldsymbol{f}(j)/(\boldsymbol{w}(j) + \boldsymbol{f}(j))$.

Low-Rank Property. Signal models based on chemical shift encoding often share the property that they yield series of images which are superpositions of only a limited number of spectral components. For the explicit case of water-fat imaging, the signal variation of a multi-echo series is a combination of water and fat images. Thus, for a series of more than two contrasts there will be a spectral sparsity. To identify this, we rewrite (1) and consider the series of contrasts as

$$\underbrace{\begin{bmatrix} \boldsymbol{x}_1(j) \\ \boldsymbol{x}_2(j) \\ \vdots \\ \boldsymbol{x}_E(j) \end{bmatrix}}_{\boldsymbol{x}(j)} = \underbrace{\begin{bmatrix} \mathrm{e}^{\mathrm{i}\boldsymbol{\Phi}(j,1)} & 0 & \cdots & 0 \\ 0 & \mathrm{e}^{\mathrm{i}\boldsymbol{\Phi}(j,2)} & \cdots & 0 \\ \vdots & \vdots & \ddots & \vdots \\ 0 & 0 & \cdots & \mathrm{e}^{\mathrm{i}\boldsymbol{\Phi}(j,E)} \end{bmatrix}}_{\boldsymbol{D}_{\Phi}(j)} \cdot \underbrace{\begin{bmatrix} 1 & c_{t_1} \\ 1 & c_{t_2} \\ \vdots & \vdots \\ 1 & c_{t_E} \end{bmatrix}}_{\boldsymbol{A}} \cdot \underbrace{\begin{bmatrix} \boldsymbol{w}(j) \\ \boldsymbol{f}(j) \end{bmatrix}}_{\boldsymbol{\rho}(j)}, \qquad (2)$$

with the chemical shift composition $\boldsymbol{A}$ and diagonal matrix $\boldsymbol{D}_\Phi$ combining relaxation and other phase effects while $\boldsymbol{\rho}$ holds the signal of water and fat.

Let $\boldsymbol{X} \in \mathbb{C}^{N \times E}$ denote the signal matrix containing all N voxels and E echos. In order to exploit the spectral sparsity, we correlate small local image regions with N_P elements of all E contrasts in a so called *Casorati* matrix $(N_P \times E)$,

$$\mathcal{B}_P(\boldsymbol{X}) = \begin{bmatrix} (\boldsymbol{D}_\Phi(p_1)\boldsymbol{A}\boldsymbol{\rho}(p_1))^T \\ \vdots \\ (\boldsymbol{D}_\Phi(p_{N_P})\boldsymbol{A}\boldsymbol{\rho}(p_{N_P}))^T \end{bmatrix}, \tag{3}$$

where $\mathcal{B}_P : \mathbb{C}^{N \times E} \to \mathbb{C}^{N_P \times E}$, $(E \ll N_P \ll N)$ denotes the reshape operator and $p_i \in \{1 \dots N\}$ is the i-th voxel from the set of voxel indices P. Besides being computationally tractable, small image regions are beneficial as we become independent of the phase error map $\boldsymbol{\Phi}$ which is expected to be rather smooth and, thus, can be assumed to be locally constant [2]. Under this assumption, the rank of this matrix is at most 2 and is in general restricted by the number of modeled spectral components: $\text{rank}(\mathcal{B}_P(\boldsymbol{X})) \leq \dim(\boldsymbol{\rho})$. The singular value distribution of sufficiently small image patches confirms this assumption in practice (see Fig. 1).
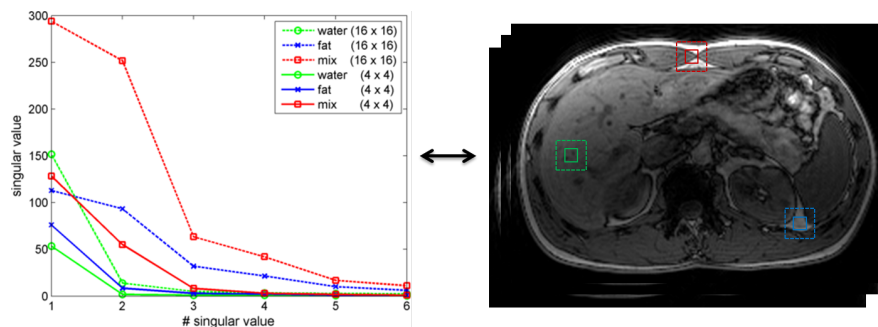

Fig. 1: Low-rank property of multi-echo MRI: Local image patches extracted from all echos yields matrices with low rank for sufficiently small patches. Note the different tissues underlying each patch and their corresponding singular value distribution.

3 Proposed Method

As we have just established, the Casorati formulation for multi-contrast water-fat MRI has a maximum rank of 2 in theory and, thus, lends itself for low-rank denoising. To this end, we find a robust estimate for the noise in the whole image domain and incorporate it into a block-wise low-rank denoising such that the optimal regularization is data-driven. Finally, a weighted averaging of the results from overlapping blocks further improves the robustness of the algorithm. We will refer to this algorithm as Robust Locally Low-Rank (RLLR) denosing.

3.1 Robust Noise Estimation

An accurate noise estimation is vital, as over- or under-estimation can render the subsequent denoising useless, especially in low SNR applications. We assume the acquired data $\hat{\boldsymbol{X}}$ to be affected by complex white noise $\mathcal{W} \overset{\text{iid}}{\sim} \mathcal{N}_{\mathbb{C}}(0, \sigma_\epsilon^2)$ and propose to combine local noise estimates from block-wise processing to a robust estimate. W.l.o.g., the set of blocks Ω tiles the spatial domain in quadratic blocks of length k as to implement a sliding window. Then we define the estimator as

$$\hat{\sigma}_\epsilon = \frac{\text{median}(\sigma_E(\mathcal{B}_P(\hat{\boldsymbol{X}})) \mid P \in \Omega_n)}{\text{median}(\sigma_E(\boldsymbol{M}_i) \mid i = 1 \ldots N_M)}, \tag{4}$$

where $\sigma_E(\cdot)$ denotes the smallest singular value of its argument and $\Omega_n \subseteq \Omega$ is a subset with every n-th block. Assuming that the lowest singular value is dominated by noise for low-rank matrices, we obtain the noise standard deviation by normalizing the median to that of random matrices sampled from the unit normal distribution $\mathcal{N}_{\mathbb{C}}(0,1)$. For the stability of the median, N_M random matrices are generated. This needs to be computed only once per block configuration.

3.2 Adaptive Block-Wise SVT

We seek to remove the noise $\boldsymbol{\mathcal{W}}$ in the acquired signal $\hat{\boldsymbol{X}}$ to obtain the pure signal $\boldsymbol{X} = \hat{\boldsymbol{X}} - \boldsymbol{\mathcal{W}}$ by processing the image domain in small partitions Ω. For blocks of locally correlated regions, the low rank property can be exploited. Rank optimization, however, is known to be NP-hard; a feasible alternative is needed. Instead of imposing hard constraints, e.g., rank-r approximation which sets all but r singular values to zero, we prefer to minimize the sum of singular values—known as the nuclear norm—for two reasons: 1) it is more robust in the sense that it will not fail when the exact rank property is violated or the modeled spectrum is enlarged and 2) as the tightest convex relaxation of the rank optimization, it can be solved efficiently [7]. Accordingly, the nuclear norm optimization for individual patches P in an unconstrained formulation reads

$$\min \frac{1}{2} \|\mathcal{B}_P(\hat{\boldsymbol{X}}) - \mathcal{B}_P(\boldsymbol{X})\|_F^2 + \lambda \|\mathcal{B}_P(\boldsymbol{X})\|_* , \lambda \geq 0, \tag{5}$$

which is the proximal operator of the nuclear norm $\|\cdot\|_*$, for which the following closed-form solution based on the singular value decomposition exists: $\text{SVT}(\mathcal{B}_P(\hat{\boldsymbol{X}}), \lambda) = \boldsymbol{U} \operatorname{diag}((\boldsymbol{\sigma} - \lambda)_+)\boldsymbol{V}^T$; $(t)_+$ is evaluated per component as $\max(t, 0)$, which performs soft-thresholding on the singular values such that values smaller than the threshold become zero while larger ones are drawn towards zero. Then, a denoised signal for the whole image can be obtained by applying SVT to each block and averaging the contribution per voxel [9]. Similarly, we define the weighted and block-adaptive denoising with individual thresholds λ_P,

$$\boldsymbol{X} = \boldsymbol{W} \circ \sum_{P \in \Omega} \mathcal{B}_P^\dagger(r_p^{-1} \operatorname{SVT}(\mathcal{B}_P(\hat{\boldsymbol{X}}), \lambda_P)), \ \boldsymbol{W} = \sum_{P \in \Omega} (\mathcal{B}_P^\dagger(r_P \boldsymbol{J}_P)) \tag{6}$$

where $\mathcal{B}_P^\dagger$ is the adjoint Casorati transform; $\boldsymbol{W}$ is the normalization matrix due to overlapping as well as weighted patches and $\boldsymbol{J}_P$ is $N_P \times E$ matrix of ones. Sparser, less noisy patches are promoted due to a reciprocal rank-weighting $r_P = \max(1, \|\boldsymbol{\sigma}_P\|_0)$ while an overlap of patches ensures data consistency [11].

The singular value threshold is critical and should be chosen robustly based on the global noise level. A noise-dependent, though fixed threshold might not be adequate for all variations in the data, i.e. the actual singular value distribution, so a block-dependent threshold may be preferred. Consequently, we make use of the SURE formulation derived by Candès *et al.* that yields the risk involved in SVT with a certain λ solely based on the data and its noise variance [9]. We propose to use adaptive risk-minimizing thresholds $\lambda_P = \mathrm{argmin}_\lambda \mathrm{SURE}(\mathcal{B}_P(\hat{\boldsymbol{X}}), \lambda, \hat{\sigma}_\epsilon^2)$ for every image block which can either be found via grid search or approximately as this function is piece-wise smooth.

4   Experiments and Results

We performed various experiments to evaluate the noise reduction of contrast images from water-fat MRI and the effects on the subsequent non-linear estimation of the clinically relevant biomarker PDFF and R_2^*. In addition, we quantified the *fit error*—introduced by the voxel-wise fitting—as further measure:

$$R_{\mathrm{fit}}(j) = \frac{\sum_e (\hat{\boldsymbol{x}}_e(j) - \boldsymbol{x}_e(j))^2}{\sum_e \hat{\boldsymbol{x}}_e(j)^2}. \tag{7}$$

Method Parameters. Throughout this study we used quadratic image patches of length $k = 5$, i.e. Casorati matrices of size $25(N_P) \times 6(E)$ as sliding windows with stride $\delta_\mathcal{B} = 1$ for all partitions of the 3-D data. Every 10-th patch was used for noise estimation. Note, the method does not require parameter tuning and is generally applicable as long as sparsity assumptions hold, i.e. $N_P \gg E$. The patch length could be chosen resolution dependent ($\sim 1\,\mathrm{cm}$), but a larger support will increase spatial smoothing while a smaller support lacks statistics and invalidates $N_P \gg E$. On standard hardware (4-core), the `C++` prototype implementation runs in under a minute for the data used here.

In-vivo Data. We used data from abdominal MRI examinations of 3 volunteers on a $3\,\mathrm{T}$ MR system (MAGNETOM Skyra, Siemens Healthcare, Erlangen, Germany). A prototype 3-D gradient multi-echo acquisition (VIBE) with PAT acceleration 4 was used in combination with the prototype of a multi-step magnitude fitting technique [10]. Parameters included TR = 16.6 ms, TEs = 1.06, 2.20, 3.69, 6.15, 9.84, 14.76 ms with flip angle = $2°$ and FoV of $420 \times 346 \times 60$ mm^3 and matrix $160 \times 132 \times 60$.

Fig. 2 shows an exemplary contrast image of a 6-echo liver examination (row 1). Comparing the original and the denoised image indicates that a constant noise bias was removed while preserving edge sharpness (left to right), which is confirmed by the difference image and by a rise in SNR[1] from 10.3 to 12.6.

---

[1] SNR is averaged over 3 smooth liver ROIs as, $\varnothing(\varnothing(|\boldsymbol{x}|)/\sigma_{(|\boldsymbol{x}|)})$.

The impact of the denoising on the biomarkers and the fit error which are obtained through fitting the echo series to the non-linear signal model are compared in row 2 & 3 of Fig. 2. PDFF, R_2^* and R_{fit} are shown left-to-right. The PDFF using the original data shows highly varying noise, possibly amplified through the fitting and the fraction calculation (SNR=3.1). The noise bias on the R_2^* map is less severe but still prominent (SNR=6.0). The fit error map indicates larger errors in the central FoV, which supports that a low SNR decreases the accuracy of the parameter estimation. The denoising, in consequence, strongly stabilizes the PDFF calculation as the fat concentration in the liver is far more homogeneous
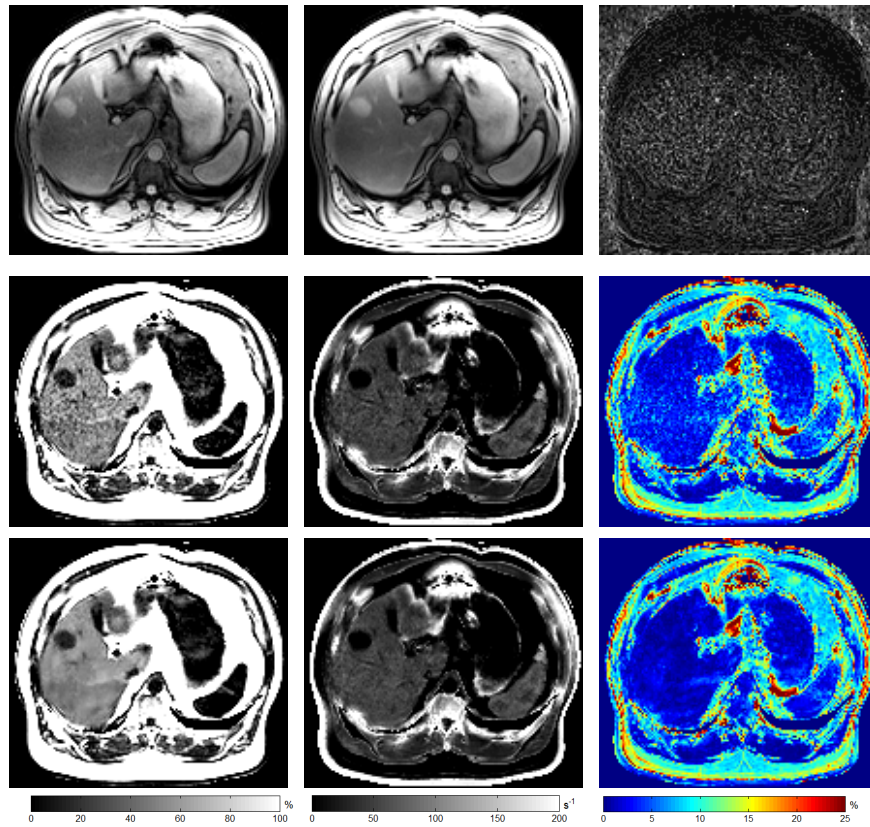

Fig. 2: Row 1: Third contrast image of a 6-echo liver fat examination with low SNR. Original (SNR=10.3), denoised (SNR=12.6) and their difference image ($20 \times$ scaled) are shown from left to right. A strong noise bias could be removed while details are enhanced, e.g., blood vessels in the liver.
Row 2 & 3: Impact of the denoising on the biomarker estimation: PDFF, R_2^* and associated fit error (left to right) using original and denoised data (bottom). Noise levels are considerably lower in PDFF (SNR=9.4, before 3.1) and R_2^* (SNR=8.4, before 6.0) maps and fit error is reduced using denoised data.

(a) $0.5\,\hat{\sigma}_\epsilon$ (b) $2\,\hat{\sigma}_\epsilon$ (c) Rank-2 approximation
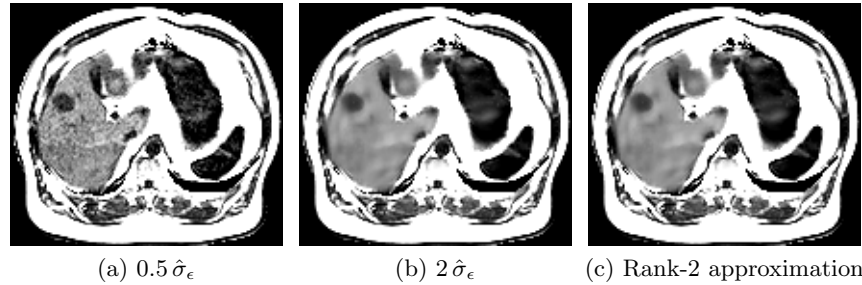
Fig. 3: Noise adaptive technique: automatically obtained noise estimate $\hat{\sigma}_\epsilon$ was altered to demonstrate under-/over regularization for inaccurate estimates (a), (b). A Rank-2 approximation yields blurred edges while our method is edge-preserving (see Fig. 2).
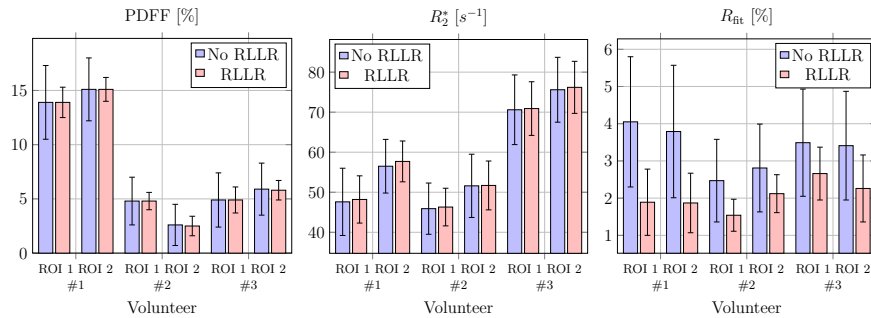

Fig. 4: Mean and standard deviation (SD) of the PDFF, R_2^* and the fit error R_{fit} for two liver ROIs of three volunteers. The SD is reduced consistently for all biomarkers, and the mean of the fit error. On average, the denoising reduced the fit error by 37 % and eliminated uncertainty (SD) of the PDFF by 58 % and that of R_2^* by 24 %.

(SNR=9.4). A milder smoothing is seen for R_2^*, though edges, e.g. blood vessels, are preserved (SNR=8.4). The fit error shows a notable decrease in regions with low signal strength, i.e. the liver and spleen. Fig. 3 demonstrates the sensitivity of the method to the noise level based on the PDFF map. When the automatically obtained noise estimate is altered, or inaccurately estimated, the method either fails to remove noise or blurs over edges. Similarly, a rank-2 approximation overshoots and removes detail. By contrast, our automatic threshold seems both edge-preserving and adaptive.

Fig. 4 shows our quantitative findings as the mean and standard deviation (SD) of the estimated biomarkers and the fit error using the original and the denoised data. For three subjects, average ROI measurements were taken from homogeneous areas of the liver for two slices, belonging to the upper and lower part of the liver. Altogether, the denoising reduced the fit error by 37 % and eliminated uncertainty (SD) of the PDFF by 58 % and that of R_2^* by 24 %.

5 Conclusion

A robust denoising algorithm for contrast-sparse MRI data has been proposed. The inherent low-rank property of locally correlated multi-contrast data is promoted with the nuclear norm in a model-consistent way. The algorithm is also automatic as the noise level is derived from local estimates of the whole image such that a risk-minimizing threshold can be used for a patch-based denoising.

We demonstrated the potential of the method on low SNR fat quantification data. Here, the contrast image series could be greatly improved while an even stronger effect is observed when this data is used for further processing, such as the fat fraction biomarker estimation. This has direct benefits as acquisition protocols with higher spatial resolution and/or lower flip angles become possible.

The integration into existing workflows is straightforward and attractive due to a low runtime and no need for parameter-tuning. Furthermore, the proposed method requires only spectrally sparse data as input and is, thus, widely applicable to instances of dynamic MRI, spectroscopy, and hyperspectral imaging.

References

1. P. Thampanitchawong and T. Piratvisuth, "Liver biopsy: complications and risk factors," *World J. Gastroenterol.*, vol. 5, pp. 301–304, 1999.
2. S. B. Reeder, Z. Wen, H. Yu, A. R. Pineda, G. E. Gold, M. Markl, and N. J. Pelc, "Multicoil dixon chemical species separation with an iterative least-squares estimation method," *Magn. Reson. Med.*, vol. 51, no. 1, pp. 35–45, 2004.
3. S. B. Reeder, I. Cruite, G. Hamilton, and C. B. Sirlin, "Quantitative assessment of liver fat with magnetic resonance imaging and spectroscopy," *J. Magn. Reson. Imaging*, vol. 34, no. 4, pp. 729–749, 2011.
4. C.-Y. Liu, C. A. McKenzie, H. Yu, J. H. Brittain, and S. B. Reeder, "Fat quantification with ideal gradient echo imaging: correction of bias from t1 and noise," *Magn. Reson. Med.*, vol. 58, no. 2, pp. 354–364, 2007.
5. P. Sharma, M. Altbach, J.-P. Galons, B. Kalb, and D. R. Martin, "Measurement of liver fat fraction and iron with mri and mr spectroscopy techniques," *Diagn Interv Radiol*, vol. 20, no. 1, pp. 17–26, 2014.
6. M. Bydder and J. Du, "Noise reduction in multiple-echo data sets using singular value decomposition," *Magn. resonance imaging*, vol. 24, no. 7, pp. 849–856, 2006.
7. J.-F. Cai, E. J. Candès, and Z. Shen, "A singular value thresholding algorithm for matrix completion," *SIAM J. on Optim.*, vol. 20, no. 4, pp. 1956–1982, 2010.
8. J. Trzasko, A. Manduca, and A. Borisch, "Local versus global low-rank promotion in dynamic mri series reconstruction," *Proc. Int. Symp. Magn. Reson. Med*, p. 4371, 2011.
9. E. J. Candès, C. A. Sing-Long, and J. D. Trzasko, "Unbiased risk estimates for singular value thresholding and spectral estimators," *IEEE Trans. Signal Process.*, vol. 61, no. 19, pp. 4643–4657, 2013.
10. X. Zhong, M. D. Nickel, S. A. Kannengiesser, B. M. Dale, B. Kiefer, and M. R. Bashir, "Liver fat quantification using a multi-step adaptive fitting approach with multi-echo gre imaging," *Magn. Reson. Med.*, vol. 72, no. 5, pp. 1353–1365, 2014.
11. J. V. Manjón, P. Coupé, A. Buades, D. L. Collins, and M. Robles, "New methods for mri denoising based on sparseness and self-similarity," *Med. image analysis*, vol. 16, no. 1, pp. 18–27, 2012.